Title	Vector piezoresponse force microscopy
Authors(s)	Kalinin, S. V.; Rodriguez, Brian J.; Jesse, S.; et al.
Publication date	2006-06
Publication information	Microscopy and Microanalysis, 12 (3): 206-220
Publisher	Cambridge University Press
Item record/more information	http://hdl.handle.net/10197/5514
Publisher's version (DOI)	10.1017/S1431927606060156

Vector Piezoresponse Force Microscopy

Sergei V. Kalinin,[1,*] Brian J. Rodriguez,[1,2] Stephen Jesse,[1] Junsoo Shin,[1,3] Arthur P. Baddorf,[1]
Pradyumna Gupta,[4] Himanshu Jain,[4,5] David B. Williams,[4] and Alexei Gruverman[6]

[1]Condensed Matter Sciences Division, Oak Ridge National Laboratory, Bldg. 3025, MS 6030, 1 Bethel Valley Rd.,
 Oak Ridge, TN 37831, USA

[2]Department of Physics, North Carolina State University, 2700 Stinson Drive, Box 8202, Raleigh, NC 27695, USA

[3]Department of Physics and Astronomy, University of Tennessee, 1408 Circle Drive, Knoxville, TN 37996, USA

[4]Department of Materials Science and Engineering, Lehigh University, 5 East Packer Avenue, Bethlehem, PA 18015, USA

[5]Center for Optical Technologies, Lehigh University, 5 East Packer Ave., Bethlehem, PA 18015, USA

[6]Department of Materials Science and Engineering, North Carolina State University, 2410 Campus Shore Drive,
 Raleigh, NC 27695, USA

Abstract: A novel approach for nanoscale imaging and characterization of the orientation dependence of electromechanical properties—vector piezoresponse force microscopy (Vector PFM)—is described. The relationship between local electromechanical response, polarization, piezoelectric constants, and crystallographic orientation is analyzed in detail. The image formation mechanism in vector PFM is discussed. Conditions for complete three-dimensional (3D) reconstruction of the electromechanical response vector and evaluation of the piezoelectric constants from PFM data are set forth. The developed approach can be applied to crystallographic orientation imaging in piezoelectric materials with a spatial resolution below 10 nm. Several approaches for data representation in 2D-PFM and 3D-PFM are presented. The potential of vector PFM for molecular orientation imaging in macroscopically disordered piezoelectric polymers and biological systems is discussed.

Key words: scanning probe microscopy, piezoresponse force microscopy, piezoelectric materials, ferroelectric materials, domains, orientation imaging

INTRODUCTION

In the last decade, piezoresponse force microscopy (PFM) has been established as a primary technique for imaging and nondestructive characterization of piezoelectric and ferroelectric materials on the nanometer scale (Eng et al., 2001; Alexe & Gruverman, 2004; Hong, 2004). The use of the electromechanical coupling at the tip–surface junction for imaging polarized regions in ferroelectric polymers was originally demonstrated by Güthner and Dransfeld (1992). This approach was later extended by Gruverman et al. (1996*a*) to nanoscale domain switching and imaging in ferroelectric thin films and single crystals. The term piezoresponse, introduced by Gruverman et al. (1996*a*) for the description of this voltage-modulated contact mode of scanning probe microscopy, comes from the fact that the measured signal is dominated by the piezoelectric deformation of the ferroelectric sample. In the original papers on PFM, only the normal component of the tip displacement related to the out-of-plane component of polarization vector has been measured, an approach further referred to as

vertical PFM (VPFM) (Gruverman et al., 1998). In 1998, Eng et al. (1998, 1999) proposed a lateral PFM (LPFM) imaging method for measuring the in-plane component of polarization by monitoring the angular torsion of the cantilever. Based on this development, an approach for three-dimensional (3D) reconstruction of polarization using a combination of the VPFM data with two LPFM data sets obtained at different scanning directions has been developed (Eng et al., 1999; Rodriguez et al., 2004). However, the lateral and vertical PFM data in these studies were generally obtained with different sensitivities and therefore could not be compared directly.

Despite this limitation, the 2D and 3D PFM imaging methods allow for the first time an insight into the domain arrangement, domain structure reconstruction, and mechanism of polarization reversal in microscopic ferroelectric capacitors. However, there is no universally accepted approach for 3D PFM imaging and data analysis and even the qualitative interpretation of 2D and 3D PFM data is subject to a large number of misconceptions.

Here, we summarize the basic principles of PFM, illustrate what information can be obtained from PFM experiments, and delineate the limitations of PFM signal interpretation. In particular, we demonstrate that the quantitative measurement of the local electromechanical re-

sponse vector (as opposed to measurements of vertical and lateral PFM maps), further referred to as vector PFM, is a unique tool for local crystallographic orientation imaging in piezoelectric materials, such as micro- and nanocrystalline ferroelectric thin films, molecular orientation in ferroelectric polymers, and biological systems. Several approaches for PFM signal calibration using external and internal standards are discussed.

PRINCIPLES OF PIEZORESPONSE FORCE MICROSCOPY

Piezoresponse force microscopy is based on the detection of the bias-induced piezoelectric surface deformation. The tip is brought into contact with the surface, and the piezoelectric response of the surface is detected as the first harmonic component, $A_{1\omega}$, of the tip deflection, $A = A_0 + A_{1\omega}\cos(\omega t + \varphi)$, induced by the application of the periodic bias $V_{tip} = V_{dc} + V_{ac}\cos(\omega t)$ to the tip. Here, the deflection amplitude, $A_{1\omega}$, is determined by the tip motion and is given in the units of length. When applied to the piezoelectric or ferroelectric materials, the phase of the electromechanical response of the surface, φ, yields information on the polarization direction below the tip. For so-called c^- ferroelectric domains (polarization vector oriented normal to the surface and is pointing downward) the application of a positive tip bias results in the expansion of the sample and surface oscillations are in phase with the tip voltage, $\varphi = 0°$, whereas for opposite c^+ domains, $\varphi = 180°$. The piezoresponse amplitude, $A = A_{1\omega}/V_{ac}$, given in the units of nm/V, defines the local electromechanical activity of the surface. The difficulty in the acquisition of PFM data stems from nonnegligible electrostatic interactions between the tip and the surface, as well as nonlocal interaction between the cantilever and the surface (Hong et al., 2001; Kalinin & Bonnell, 2001, 2004; Huey et al., 2004). In the general case, the measured piezoresponse amplitude can be written as $A = A_{el} + A_{piezo} + A_{nl}$, where A_{el} is the electrostatic contribution, A_{piezo} is the electromechanical contribution, and A_{nl} is the nonlocal contribution due to capacitive cantilever–surface interaction (Hong et al., 2001; Kalinin & Bonnell, 2002; Harnagea et al., 2003; Huey et al., 2004). Quantitative PFM imaging requires A_{piezo} to be maximized to achieve predominantly electromechanical contrast. Provided that the phase signal varies by 180° between domains of opposite polarities, indicative of a small capacitive crosstalk contribution to the signal, PFM images can be conveniently represented as $A_{1\omega}\cos(\varphi)/V_{ac}$, where $A_{1\omega}$ is the amplitude of first harmonic of measured response. Experimentally, the collected signal is the output of the lock-in amplifier, and we refer to the experimental signal as $PR = aA_{1\omega}\cos(\varphi)/V_{ac}$, given in the units of [V], where a is a calibration constant determined by the lock-in settings and sensitivity of the photodiode. The unique feature of the

scanning probe-based techniques is that, in addition to the vertical displacement, torsion of the cantilever can be measured as well, thus allowing measurement of both VPFM and LPFM signals as illustrated in Figure 1. Note that in general vertical and lateral sensitivities of PFM are different, and several approaches for calibration have been suggested (Peter et al., 2005). In general, separate recording of amplitude, $|PR|$, and phase, φ, images is a more sensitive mode of microscope operation.

For future discussion of the PFM image formation mechanism, we recall the basic principles of atomic force microscopy (AFM) (Sarid, 1991). The vertical displacement of the tip, w_3^t, results in the bending of the cantilever by angle $\theta_d \sim w_3^t/L$, where L is the cantilever length (Fig. 2a). The deflection of the laser beam reflected from the cantilever is detected by the split photodiode. Under normal contact mode imaging conditions, the AFM employs a feedback loop to keep the cantilever deflection at a set-point value by adjusting the height of the cantilever base while scanning. This feedback signal thus provides a topographic image of the surface, which is relatively insensitive to the exact details of cantilever and tip motion. However, PFM imaging is based on the direct measurement of the changes in cantilever angle. For purely vertical motion of the tip (Fig. 2a), the measured photodiode signal can be directly related to the tip displacement using a suitable calibration procedure, because $A = w_3^t$. However, an additional contribution to the deflection signal will originate from the buckling oscillations of the cantilever, as illustrated in Figure 2b. Although these oscillations do not change the position of the tip, the change in the deflection angle will be recorded as apparent height contrast. Buckling of the cantilever is the primary source of the nonlocal electrostatic signal contribution to the PFM contrast and can be reduced by using sufficiently stiff cantilevers (Kalinin & Bonnell, 2004). Similarly, the longitudinal motion of the tip end, w_1^t, will also result in the cantilever bending $\theta_d \sim w_1^t/H$, where H is the tip height. This nontrivial detection mechanism must be taken into account in the interpretation of the PFM data as discussed below.

ELECTROMECHANICAL MEASUREMENTS BY PFM

In the general case of a piezoelectric sample with arbitrary crystallographic orientation, application of the bias to the tip results in the surface displacement, $\mathbf{w}$, with both normal and in-plane components, $\mathbf{w} = (w_1, w_2, w_3)$. The usual assumption in the interpretation of PFM data is that the displacement of the tip apex in contact with the surface is equal to the surface displacement, $\mathbf{w}_t = \mathbf{w}$. It has been shown that this is generally true for the normal component of the tip displacement, $w_3^t = w_3$ (Karapetian et al., 2005), because the effective spring constant of the tip–surface junction is typically 2–3 orders of magnitude higher than

$$V_{tip} = V_{dc} + V_{ac} \sin \omega t$$
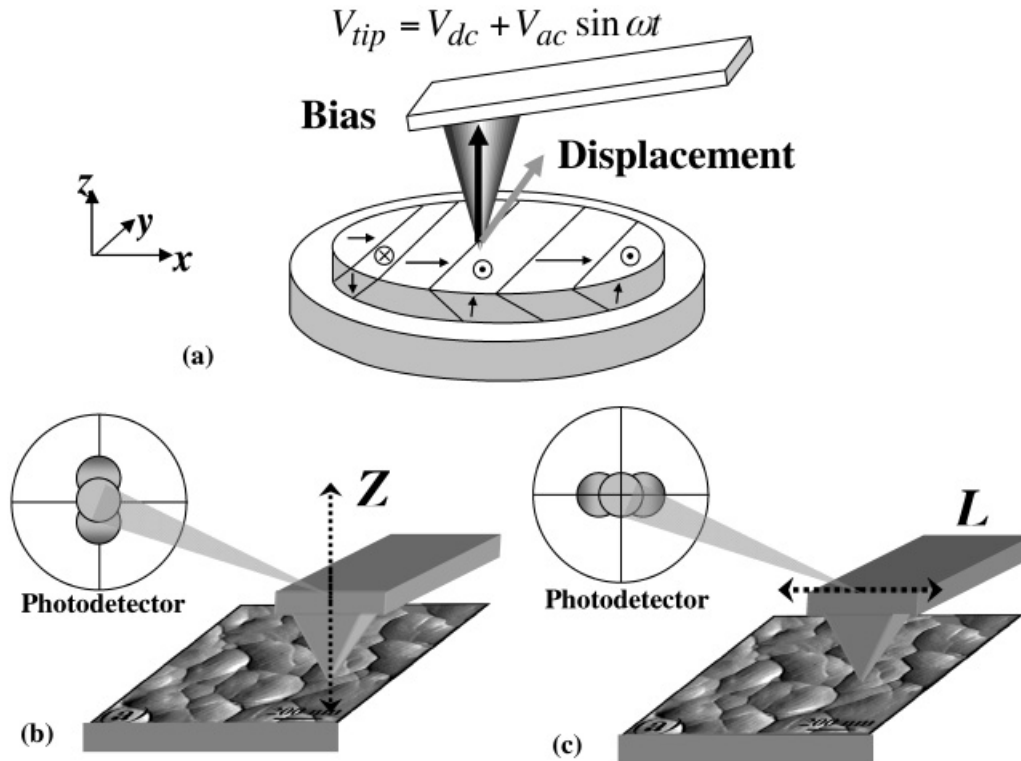
Figure 1. a: Vector nature of the electromechanical response. Schematics of vertical (**b**) and lateral (**c**) PFM detection.

the cantilever spring constant. This approximation breaks down in the cases when the spring constant of the tip–surface junction becomes comparable to the spring constant of the cantilever, when, for example (a) PFM imaging of soft materials, such as ferroelectric polymers or biological systems, with large spring constant cantilevers or (b) PFM imaging at frequencies well above the first resonance frequency of the cantilever when the dynamic stiffening effects are important.

Alternatively, amplification of the effective PFM signal is possible due to the resonance enhancement or the onset of the regime when the tip loses contact with the surface, when, for example (c) PFM imaging at the cantilever resonances or (d) using high modulation amplitudes.

These phenomena can be adequately described using dynamic models that take into account the frequency-dependent oscillatory behavior of the cantilever. The linear model (tip oscillation magnitude is proportional, rather then equal, to surface displacement) then can be still applied using a proper calibration approach, provided that dynamic characteristics of the system (e.g., spring constant of the tip–surface junction) do not vary.

The origins of the in-plane component of electromechanical response are much less understood. It is generally agreed that the use of a conventional four-quadrant photodetector allows the lateral piezoresponse component in the direction normal to the cantilever axis (lateral transversal displacement) to be determined as torque of the cantilever. Thus, if the cantilever orientation is given by the vector $n =$ $(\cos \theta_c, \sin \theta_c, 0)$, where θ_c is the angle between the long axis of the cantilever and x-axis of the laboratory coordinate system, the lateral PFM signal is proportional to the projection of the surface displacement on the vector perpendicular to the cantilever axis, $PR_p = b(-w_1 \sin \theta_c + w_2 \cos \theta_c)$ (Fig. 2c). For a low-symmetry surface, the relationship between the piezoresponse and surface displacement can be more complex and b can be a second rank tensor; however, due to the difficulty in determining the relevant parameters, such description is unlikely to be practical.

The fundamental difference between VPFM and LPFM is that in the latter case the displacement of the tip apex can be significantly smaller than that of the surface, for example, due to the onset of sliding friction (Bdikin et al., 2004). Therefore, whereas in VPFM the response amplitude is expected to scale linearly with the modulation amplitude, in LPFM the response amplitude will eventually saturate.

Another issue in the LPFM imaging, which, to our knowledge, has not yet been reported,[1] is the presence of the piezoresponse component along the cantilever axis (longitudinal displacement), $PR_l = c(w_1 \cos \theta_c + w_2 \sin \theta_c)$, as illustrated in Figure 2d. As discussed above, the vertical displacement of the cantilever is measured through the deflection angle of the cantilever, $\theta_d \sim h/L$, where L is cantilever length. Surface displacement along the cantilever axis will also result in the change of deflection angle. If the surface

---

[1]This effect is partially considered by Abplanalp (2001).
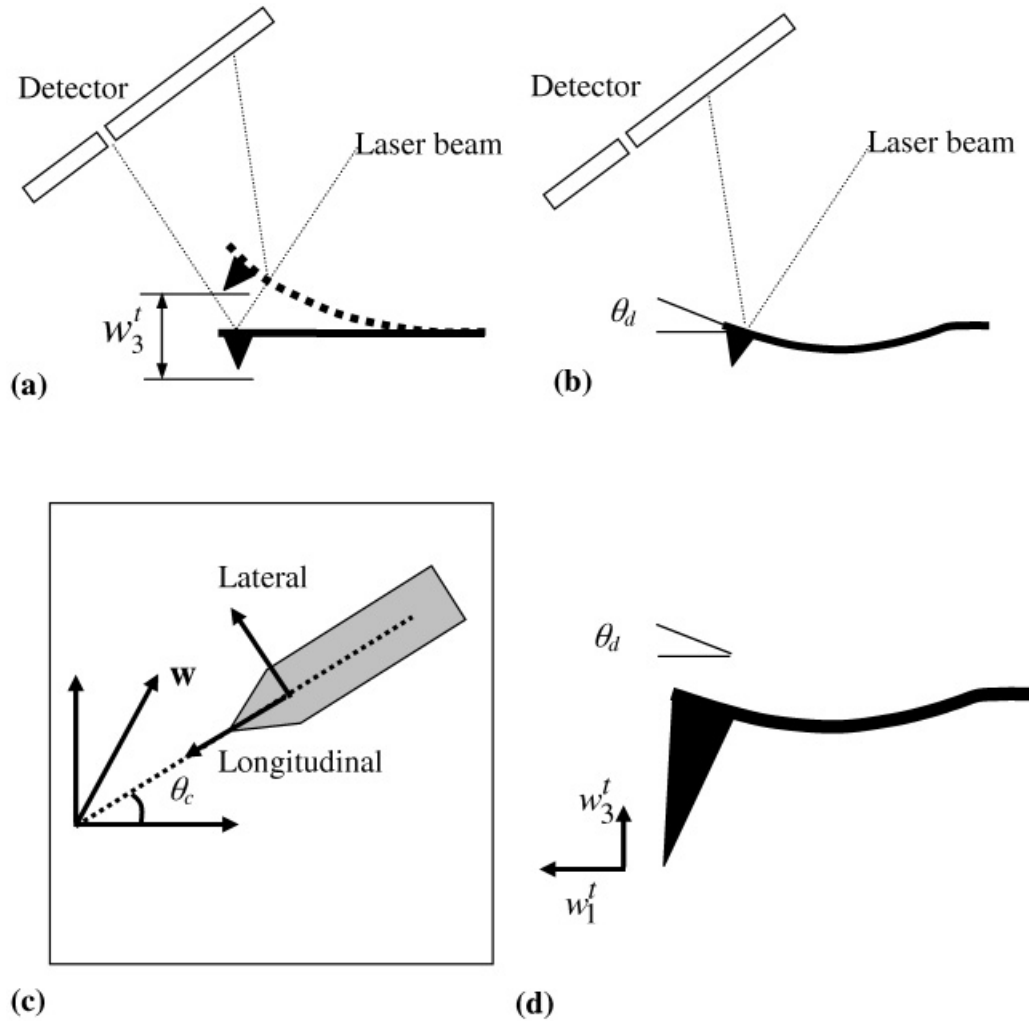
Figure 2. a: Vertical tip displacement in beam-deflection AFM is achieved through the detection of cantilever deflection angle. **b:** Distributed force results in cantilever buckling and change in the deflection angle, detected as apparent tip-height change. **c:** Contributions to cantilever deflection. In-plane cantilever orientation in the arbitrary laboratory coordinate system including lateral (perpendicular to the cantilever axis) and longitudinal (along the cantilever axis) components. **d:** Longitudinal surface displacement along the long cantilever axis results in the change in deflection angle, providing contribution to the VPFM signal.

displacement and the tip displacement are equal, the deflection angle is $\theta_d \sim h/H$, where H is tip height. Given that typically $H \ll L$, this implies that the "vertical" PFM signal is more sensitive to the lateral longitudinal surface displacement than the vertical surface displacement! This difference in signal transduction mechanism is also observed for lateral PFM signal (Peter et al., 2005); however, unlike longitudinal and vertical modes, the coupling between normal and torsional modes of rectangular cantilever oscillations is generally weak (Jeon et al., 2004) and can be ignored.

On close inspection of existing experimental data on model systems (Abplanalp, 2001; Ganpule, 2001; Harnagea 2001; Kalinin 2002), such as a and c domains on BaTiO$_3$ (100) surface, a nonzero VPFM signal can in some cases be observed over a-domain regions with in-plane polarization. However, this signal is much weaker than that in c-domain

regions. Although a complete description of this behavior is unavailable, it can be argued that the longitudinal surface displacement is not effectively transmitted to the cantilever due to the onset of sliding. This contribution of the lateral longitudinal surface displacement to the vertical signal can be determined from comparison of VPFM images obtained for different cantilever orientations in the X–Y plane as discussed below.

It is important to emphasize that the simple combination of VPFM and LPFM measurements is insufficient to unambiguously determine the 3D piezoresponse vector for an arbitrarily oriented sample. Indeed, in the general case, all three component of $\mathbf{w} = (w_1, w_2, w_3)$ are unknown. The VPFM signal is $PR_v = aw_3 + c(w_1 \cos \theta_c + w_2 \sin \theta_c)$, whereas the LPFM signal gives information on the linear combination of in-plane components, $PR_l = b(-w_1 \sin \theta_c + w_2 \cos \theta_c)$.

Generally the proportionality coefficients between the displacement vector and the measured signal are unknown and are different for vertical and lateral PFM (Peter et al., 2005), that is, $a \neq b$, thus providing an additional limitation on data interpretation. Hence, we suggest that complete 3D reconstruction of electromechanical response vector from VPFM and LPFM data is possible only if $c \ll a$, that is, the contribution of the surface displacement along the cantilever axis to the VPFM signal is small, and the following conditions are fulfilled:

1. Absolute vertical and lateral sensitivities are carefully calibrated (e.g., using approach for friction force microscopy calibration by Ogletree et al., 1996, and More et al., 2005, or calibrated piezoactuators by Peter et al., 2005), and the material is electromechanically homogeneous, that is, $|\mathbf{w}| = const$ for existing domains, providing the third equation to determine components of $\mathbf{w}$.
2. The number of possible orientations of polarization vectors is known and limited.

The latter case may include single crystals cut along the major crystallographic planes, such as BaTiO$_3$ (100) with six possible polarization orientations, epitaxial thin films, or textured polycrystalline films with well-defined crystallographic orientation (e.g., PZT films in a tetragonal phase). Although the knowledge of the crystallographic structure of material is sufficient to reconstruct the polarization orientation in single crystals, this task is more challenging in thin films and ceramic materials with random grain orientation (Roelofs et al., 2000; Munoz-Saldana et al., 2003). In addition, information on the response component along the cantilever is usually difficult to obtain and in most cases only a 2D image can be acquired. The reason is that the sample has to be physically rotated with respect to the cantilever, as a simple change of the scan angle will not produce this result. This requirement significantly limits the applicability of this approach, because it necessitates locating the same microscale region on the surface after sample rotation, a task that is possible only for the samples with clear microscopic topographic markers.

Complete 3D reconstruction of the polarization vector has been performed by Eng et al. (1999) for a barium titanate crystal using a combination of lateral and vertical PFM. Well-defined water marks on the surface were used as position markers. Rodriguez et al. (2004) have suggested using this approach for 3D polarization reconstruction in micrometer-size (111)-oriented PZT capacitors. In this case, sequential acquisition of two LPFM images at two orthogonal orientations of the sample with respect to the cantilever, further referred to as x-LPFM and y-LPFM images, has been accomplished by using the etched top electrodes as topographic markers.

During these measurements, the laboratory coordinate system is selected such as $\theta_c = 0$ for x-PFM and $\theta_c = \pi/2$ for y-PFM. Thus, the x-LPFM signal is $xPR_l = bw_2$, the corresponding vertical PFM signal is $xPR_v = aw_3 + cw_1$, the y-LPFM signal is $yPR_l = bw_1$, and the y-VPFM signal is $yPR_v = aw_3 + cw_2$. Note that for the flat and mechanically isotropic surface the proportionality coefficient, b, between the measured LPFM signal and the surface displacement can be assumed to the same for both x-LPFM and y-LPFM measurements. Thus, the relationship between measured piezoresponse signals and the surface displacement vector is

$$\begin{pmatrix} xPR_v \\ xPR_l \\ yPR_v \\ yPR_l \end{pmatrix} = \begin{pmatrix} c & 0 & a \\ 0 & b & 0 \\ 0 & c & a \\ b & 0 & 0 \end{pmatrix} \begin{pmatrix} w_1 \\ w_2 \\ w_3 \end{pmatrix}. \tag{1}$$

This analysis can be extended for nonorthogonal scan directions in a straightforward manner. For known a and b, equation (1) allows the contribution of the longitudinal displacement to the VPFM signal to be determined from the ratio $\beta = (xPR_v - yPR_v)/(xPR_v + yPR_v)$, a spatial map of which allows the contribution of longitudinal surface displacement to the VPFM signal to be determined. If $\beta \ll 1$ within the image, the VPFM signal is artifact free.

In the future analysis, we will assume that vertical PFM does not contain a significant contribution from the longitudinal surface displacement, as suggested by experimental observations (e.g., vertical PFM signal is typically small for in-plane domains, etc.). In this case, x-VPFM and y-VPFM images are identical, $xPR_v = yPR_v = vPR$, and equation (1) becomes

$$\begin{pmatrix} xPR_l \\ yPR_l \\ vPR \end{pmatrix} = \begin{pmatrix} 0 & b & 0 \\ b & 0 & 0 \\ 0 & 0 & a \end{pmatrix} \begin{pmatrix} w_1 \\ w_2 \\ w_3 \end{pmatrix}. \tag{2}$$

Equation (2) contains two independent calibration constants, a and b. The calibration constant for the VPFM signal, a, can be determined in a straightforward way by using an external reference, for example, a piezoelectric sample with well-known piezoelectric constants, such as quartz, in the integral excitation (metal-coated top surface) configuration (Christman et al., 1998; Ganpule, 2001, Peter et al., 2005). Alternatively, the sample can be mounted on a calibrated piezoelectric transducer and surface vibration at low frequencies below the cantilever and transducer resonances can be used to calibrate the tip oscillation amplitude. The calibration constant for lateral PFM is generally unknown and strongly depends on the properties of the tip–surface contact (e.g., sliding, tip wear, etc.). Two approaches for lateral PFM calibration, that is, determination of constant b, can be considered. In the first case, the LPFM signal is measured on the material with known properties (e.g., BaTiO$_3$ (100)) and the linearity of response with driving amplitude (i.e., absence of sliding friction) is verified. This approach is limited by the lack of exact solutions for lateral deformation

in PFM geometry (an approach for semiquantitative interpretation of LPFM data is presented in the section on crystal orientation effects below) and high sensitivity to surface conditions. In the second case, the sample is mounted on the shear oscillator and surface displacement is then calibrated self-consistently, similar to the VPFM case, as recently demonstrated by Peter et al. (2005).

An alternative approach for relative calibration of sensitivities of VPFM and LPFM signals (i.e., determination of the a/b ratio, rather then absolute values of these constants) is based on an internal calibration standard, utilizing the fact that PFM provides an image, rather than a single-point measurement. Provided that partial information on material structure is available, magnitudes of VPFM and LPFM signal from different regions can be compared. For example, for a BaTiO$_3$ (100) surface with a cantilever oriented along the (010) axis, the VPFM signal is nonzero in c-domains, whereas the LPFM signal is nonzero for the a domain. Because the absolute values of the electromechanical response in these cases are known, the relative sensitivities of LPFM and VPFM can be determined by comparing the signal strength from different regions and then used for imaging, for example, ceramics with an unknown crystallographic orientation. A similar approach can be applied for systems with a finite number of known crystallographic orientations, when the PFM response corresponding to the dominant orientation can be determined as the maxima on the statistical response histograms.

Thus, the following approaches to the PFM measurements are possible, depending on the dimensionality of the obtained data set (1D, VPFM; 2D, VPFM and LPFM; 3D, VPFM and x, y-LPFM), knowledge of the relative calibration of VPFM and LPFM data (i.e., the a/b ratio is known), and absolute calibration (a and b are known). In the case of 2D and 3D PFM, relative calibration of vertical and lateral signals allows combining them to produce an electromechanical vector field, an approach we refer to as vector PFM. The following cases are possible:

1. VPFM: Only a normal component of the surface displacement vector is measured. This method provides comprehensive information on piezoelectric activity for uniaxial crystals and thin films with the polar axis normal to the film surface.
2. 2D-PFM: VPFM and complementary x-LPFM images are acquired. The normal component of the piezoresponse vector and the transversal component of the in-plane piezoresponse (normal to the cantilever axis) are mapped. The longitudinal component of the in-plane piezoresponse (along the cantilever axis) is unknown. If the relative calibrations of VPFM and LPFM are unknown, these measurements provide complementary maps of the vertical and lateral electromechanical response. If the VPFM and LPFM data are calibrated (2D vector PFM), they can be combined to form a quantitative 2D electromechanical vector map.
3. 3D-PFM: VPFM, x-LPFM, and y-LPFM images are acquired. All three components of the piezoresponse vector are known. If the relative calibrations of VPFM and LPFM are unknown, these measurements provide complementary maps of the vertical and lateral electromechanical response. The in-plane data sets can be combined to form an in-plane 2D vector map. If the lateral and vertical signals are calibrated (3D vector PFM), a complete description of the local electromechanical response is obtained.

Note that in 2D and 3D vector PFM, calibration of the response components, using, for example, an external oscillator or internal standard, allows maximizing the amount of information the experiment provides. In some cases, the system can be overdetermined if additional constraints on the response vector exist. For example, for electromechanically homogeneous materials, the condition $w_1^2 + w_2^2 + w_3^2 = const$ provides an additional constraint and a combination of VPFM, x-LPFM, and y-LPFM is now sufficient to completely reconstruct the displacement vector, even if calibration, that is, the a/b ratio, is unknown. For the vast majority of ferroelectric and piezoelectric materials, for which the magnitude of electromechanical response vector is orientation dependent, the a/b ratio must be known for rigorous 3D reconstruction of the response vector.

RELATIONSHIP BETWEEN MECHANICAL DISPLACEMENT AND MATERIALS PROPERTIES

The next step in the interpretation of the PFM data is detailed analysis of materials properties that can be extracted from the displacement vector. Assuming the scanning probe microscope is calibrated, the set of the piezoresponse data can be converted into the full electromechanical response vector, $\mathbf{w} = (w_1, w_2, w_3)$. Here, we discuss what information on local materials properties can be obtained using this approach. In the following discussion, we assume that the PFM is calibrated and $vPR = w_3/V_{ac}$, $xPR_l = w_2/V_{ac}$, and $yPR_l = w_1/V_{ac}$ now correspond to surface displacement amplitudes in the laboratory coordinate system linked to cantilever orientation introduced in the preceding section.

The piezoelectric properties of materials are described by the third-order piezoelectric constant tensor, d_{ij}, where $i = 1, \ldots, 3, j = 1, \ldots, 6$, that defines the relationship between the strain tensor and the electric field: $X_j = d_{ij}E_i$ (Cady, 1964; Nye, 1985). Here, the components of d_{ij} are given in the laboratory coordinate system in which axis 3 is normal to the surface and axis 1 is oriented along the long cantilever axis and the reduced Voigt notation[2] is used.

---

[2] Due to symmetry, the indices i, j in full piezoelectric coefficient tensor, d_{ijk}, and strain tensor, X_{ij}, can be substituted as $11 \rightarrow 1$, $22 \rightarrow 2$, $33 \rightarrow 3$, $12 \rightarrow 6$, $13 \rightarrow 5$, $23 \rightarrow 4$.

The piezoresponse signal measured in the PFM experiment has the same dimensionality as piezoelectric constants, suggesting the close relationship between d_{ij} and components of the electromechanical surface response vector. This is remarkable, because PFM is thus an SPM technique that is sensitive to the tensorial properties of materials. However, this relationship also greatly complicates data interpretation, as discussed below.

For example, the piezoelectric constant d_{33} determines the mechanical response in the z direction due to the electric field in the z direction and is typically identified with the VPFM signal (Gruverman et al., 1996b; Rodriguez et al., 2004). For the same tip-sample geometry, the x-LPFM signal was proposed to be related to d_{32} (displacement in the y direction due to the field in the z direction) and the y-LPFM signal to be proportional to d_{31} (displacement in the x direction due to the field in the z direction). However, LPFM measurements of the vertically oriented c domains in BaTiO$_3$ (100), for which $d_{31} = d_{32} \neq 0$, show that x-LPFM and y-LPFM signals are identically zero; this behavior can also be expected from symmetry arguments.

To resolve this apparent inconsistency, we recall that strain and displacement are not equivalent, and, in general, the strain tensor is related to the component of the displacement vector, $\mathbf{u} = (u_1, u_2, u_3)$, as

$$
X_{ij} = \begin{pmatrix}
\dfrac{\partial u_1}{\partial x_1} & \dfrac{1}{2}\left(\dfrac{\partial u_1}{\partial x_2} + \dfrac{\partial u_2}{\partial x_1}\right) & \dfrac{1}{2}\left(\dfrac{\partial u_1}{\partial x_3} + \dfrac{\partial u_3}{\partial x_1}\right) \\
\dfrac{1}{2}\left(\dfrac{\partial u_1}{\partial x_2} + \dfrac{\partial u_2}{\partial x_1}\right) & \dfrac{\partial u_2}{\partial x_2} & \dfrac{1}{2}\left(\dfrac{\partial u_2}{\partial x_3} + \dfrac{\partial u_3}{\partial x_2}\right) \\
\dfrac{1}{2}\left(\dfrac{\partial u_1}{\partial x_3} + \dfrac{\partial u_3}{\partial x_1}\right) & \dfrac{1}{2}\left(\dfrac{\partial u_2}{\partial x_3} + \dfrac{\partial u_3}{\partial x_2}\right) & \dfrac{\partial u_3}{\partial x_3}
\end{pmatrix}.
$$

(3)

Therefore, relating the displacement to the electric field requires the system of partial differential equations (3) to be solved for proper boundary conditions. For an ideal case of a uniform electric field in the z direction, that is, $\mathbf{E} = \mathbf{z}E_3$, the strain components are $X_j = d_{j3}E_s$, $j = 1,\ldots,6$. For the rectangular symmetric piezoelectric block, the displacement at the center is $\mathbf{u} = (d_{35}V, d_{34}V, d_{33}V)$, as derived in Appendix A. Thus, for this model geometry, the VPFM signal is indeed determined by the piezoelectric constant d_{33}, $vPR = d_{33}$, whereas the LPFM signals are determined by the shear components of the piezoelectric constant tensor, $xPR_l = d_{35}$ and $yPR_l = d_{34}$, and the components d_{31} and d_{32} result in axially symmetric deformation of material that does not contribute to displacement at the center.

Currently, there are two main paradigms in PFM measurements. First, in the local excitation case, the bias is applied to the SPM tip that acts as a movable top electrode. The electric field in this case is highly nonuniform and reminiscent of that produced by the point charge. Second, in the integral excitation case, the bias is applied to a deposited top electrode in contact with the SPM tip, thus generating a uniform electric field in the sample. In both cases, the SPM tip acts as a sensor for the local surface displacement (Gruverman, 2004).

The rigorous solution for image formation mechanism in PFM in the local excitation case was obtained by Kalinin et al. (2004) using the exact solutions for piezoelectric indentation developed by Karapetian and Kachanov (Karapetian et al., 2002, 2005). This solution is currently available only for transversally isotropic materials, corresponding to such systems as c^+-c^--domain structure in BaTiO$_3$, periodically poled LiNbO$_3$, and other uniaxial ferroelectric crystals. In these cases, the lateral response is zero due to symmetry, $xPR_l = yPRI = 0$. The numerical analysis of the exact solution for the vertical PFM signal has shown that, for a broad range of materials, the absolute value of the piezoresponse signal is close to the d_{33}, with the deviation from this value being most significant for materials with strong anisotropy of the dielectric constant tensor. Thus, the approximation of $vPR_l = d_{33}$, although, strictly speaking, being incorrect, does provide a good first approximation. An improved simple estimation taking into account the electric field distribution in the material was obtained by Rabe et al. (2002). For materials with lower symmetry, the LPFM signal is nonzero. Although the exact analytical solutions are no longer available for these cases, following the analogy with VPFM, the estimate $xPR_l = d_{35}$ and $yPR_l = d_{34}$ can be assumed to provide a first approximation for the description of the LPFM data, even though either analytical solutions or numerical simulations are required to prove this conjecture.

In the integral excitation case, the electric field is essentially uniform. For continuous thin films, the mechanical constraints at the bottom film interface will result in the renormalization of the effective piezoelectric constants as analyzed by Ouyang et al. (2004). The PFM signal in this case will be expressed through the components of the renormalized d_{ij} tensor, which now accounts for mechanical constraints (zero strain in the film plane). For patterned ferroelectric structures, such as etched nanoislands (Ganpule et al., 1999), the difference in the mechanical conditions in the center of the island and on the circumference can result in a complex response, including a change in substrate geometry, and so forth (Nagarajan et al., 2003; Li et al., 2004). This effect can be easily understood from the example in Appendix A, which shows that the contribution from the piezoelectric constants d_{31} and d_{32} to the displacement in an arbitrary point (off-center) of the piezoelectric island is nonzero.

To summarize, in the local excitation case, the PFM signal can be semi-quantitatively approximated as $vPR_l = d_{33}$, $xPR_l = d_{35}$, and $yPR_l = d_{34}$, where the coordinate system for d_{ij} is the laboratory coordinate system related to the cantilever orientation. This interpretation is rigorous for the continuous thin films in the integral excitation case, but the elements of d_{ij} are now renormalized to account for mechanical constraints at the bottom interface. For patterned ferroelectrics, the response can be significantly af-

fected by the difference in the local elastic constraints in the different parts of the nanostructure, and numerical calculations, taking into account substrate effects, are generally required to model the electromechanical response.

CRYSTAL ORIENTATION EFFECTS

In the discussion above, the local electromechanical response vector, $\mathbf{w} = (w_1, w_2, w_3)$, was related to the elements of the piezoelectric tensor, d_{ij}, taken in the laboratory coordinate system. However, it is conventional to represent the piezoelectric constant tensor in the coordinate system related to the orientation of crystallographic axis of the material, d_{ij}^0. In this case, the intrinsic material symmetry will limit the number of nonzero components and, more importantly, allow the material-specific values to be tabulated.

The effect of crystallographic orientation on VPFM images was studied by Harnagea et al. (2001) who extended the formalism developed by Du et al. (1997) to the VPFM signal. Assuming that $vPR = d_{33}$, the effective PFM signal can be related to crystal orientation using a coordinate transformation that aligns the z-axis of the crystal coordinate system with the z-axis of the laboratory coordinate system using two rotation angles (Harnagea, 2001).

However, this approach is insufficient for the description of the LPFM image formation mechanism. Indeed, in the general case, a complete description of the coordinate transformation requires three rotations described by the Euler angles ϕ, θ, and ψ, as described in Appendix B (Newnham, 2005). Here we use the definition for which identity transformation corresponds to $\phi = \theta = \psi = 0$, as opposed to definition by Harnagea where identity corresponds to $\theta = \pi/2$ and $\varphi = 0$.

In the general case, the relationship between the d_{ij} tensor in the laboratory coordinate system and the d_{ij}^0 tensor in the crystal coordinate system is (Newnham, 2005)

$$d_{ij} = A_{ik} d_{kl}^0 N_{lj}, \tag{4}$$

where the elements of the rotation matrices N_{ij} and A_{ij} are given in Appendix B.

As an example, we consider a and c domains in tetragonal BaTiO$_3$. In the coordinate system oriented along the crystal c-axis, the d_{ij}^0 tensor is

$$d_{ij}^0 = \begin{pmatrix} 0 & 0 & 0 & 0 & d_{15}^0 & 0 \\ 0 & 0 & 0 & d_{15}^0 & 0 & 0 \\ d_{31}^0 & d_{31}^0 & d_{33}^0 & 0 & 0 & 0 \end{pmatrix}. \tag{5}$$

For the laboratory coordinate system chosen such that the (100) crystallographic orientation coincides with the cantilever axis, for the c^+ domain, the laboratory and crystallographic coordinate systems coincide and $d_{ij} = d_{ij}^0$. Cor-

respondingly, $vPR = d_{33}^0$ and $xPR_l = yPR_l = 0$. For the a_2 domain with polarization in the (010) direction oriented perpendicular to the cantilever axis, the relationship between coordinate systems is given by rotation angles $\phi = 0$, $\theta = \pi/2$, $\psi = 0$, and the elements of d_{ij} tensor are

$$d_{ij} = \begin{pmatrix} 0 & 0 & 0 & 0 & 0 & d_{15}^0 \\ d_{31}^0 & d_{33}^0 & d_{31}^0 & 0 & 0 & 0 \\ 0 & 0 & 0 & d_{15}^0 & 0 & 0 \end{pmatrix}. \tag{6}$$

Correspondingly, $vPR = 0$, $xPR_l = d_{15}^0$, and $yPR_l = 0$, recovering the early assumption of $xPR_l = d_{15}^0$ (Eng et al., 1998). For a_1 domain oriented along the cantilever axis, $\phi = 0$, $\theta = \pi/2$, $\psi = \pi/2$, and PFM components are $vPR = 0$, $xPR_l = 0$, and $yPR_l = d_{15}^0$, as expected. For a general orientation of the crystal, the response components are

$$d_{33} = (d_{15} + d_{31})\sin^2\theta\cos\theta + d_{33}\cos^3\theta \tag{7a}$$

$$d_{34} = -(d_{31} - d_{33} + (d_{15} + d_{31} - d_{33})\cos 2\theta)\cos\psi\sin\theta \tag{7b}$$

$$d_{35} = -(d_{31} - d_{33} + (d_{15} + d_{31} - d_{33})\cos 2\theta)\sin\psi\sin\theta \tag{7c}$$

Note that the response is independent of ϕ, indicative of the rotational symmetry of tetragonal BaTiO$_3$ along the 3-axis.

Equation (4) has several broad implications for materials characterization by PFM, depending on what additional information on the material's structure and properties is available. When the crystallographic orientation of the sample is known exactly, the vector VPFM, 2D-PFM, or 3D-PFM measurements allow semiquantitative evaluation of all the elements of the d_{ij}^0 tensor. For materials with high symmetry, for which only several elements of the d_{ij}^0 tensor are nonzero, they can be determined semi-quantitatively at each point using vector VPFM data (one nonzero element) and 2D and 3D-PFM data (two and three nonzero elements, respectively).

When the exact crystallographic orientation of the sample is unknown, but the number of possible polarization orientations is small, the local polarization orientation can be obtained from a thorough analysis of VPFM, 2D-PFM, or 3D-PFM data. One of the few successful reconstructions of 3D domain structure from PFM data to date belongs to this case (Eng et al., 1999; Rodriguez et al., 2004); however, no attempts to derive piezoelectric coefficients other than d_{33} have been reported. In some cases, 2D- and/or 3D-PFM combined with the partial information on local crystallographic orientation derived from known constraints on possible orientation of non-180° domain walls have been used to semi-quantitatively characterize domain structure in poly-

crystalline materials. However, in this case there is a high degree of uncertainty in determining the components of d_{ij}^0.

Finally, for the case where the sample has an arbitrary crystallographic orientation, the individual components of the d_{ij}^0 tensor cannot be determined. However, for materials with known d_{ij}^0 values, a reverse problem can be solved from the 3D vector PFM data. The local crystallographic orientation, $(\phi_i, \theta_i, \psi_i)$, can be derived, providing an approach for nanoscale orientation imaging. The applications of this approach for several materials systems will be reported elsewhere (Kalinin et al., 2006) and are beyond the scope of this article. Notably, rigorous orientation imaging by PFM is possible if and only if a properly calibrated vector 3D-PFM data set is available and piezoelectric constants d_{ij}^0 for the material are known; that is, the number of unknowns, (ϕ, θ, ψ), is equal to the number of measured parameters, (vPR, xPR_l, yPR_l). In this case, the approximations introduced in the preceding section can be further removed by numerical calculation of the orientation dependence of VPFM and LPFM signals. In the general case, VPFM, 2D-PFM, and noncalibrated 3D-PFM data are insufficient for complete reconstruction of the local crystallographic orientation unless additional constraints on the local piezoelectric response vector are present.

To summarize, the orientation dependence of the local electromechanical response that can be completely or partially determined by the PFM experiment is given by equation (4). For materials with known crystallographic orientation, the elements of the d_{ij}^0 tensor can be semi-quantitatively determined by VPFM and vector 2D- or 3D-PFM measurements performed on crystals with different orientations. For materials with known piezoelectric constants, d_{ij}^0, the local crystallographic orientation in each point (electromechanical orientation imaging) can be determined from vector 3D-PFM data. For materials systems with known constraints on possible crystallographic orientation (a small number of domains), domain structure reconstruction can be obtained from partial VPFM or 2D-PFM data.

POLARIZATION ORIENTATION FROM PFM DATA

The original motivation for the development of PFM was the necessity for nondestructive imaging of the local polarization vector, $\mathbf{P} = (P_1, P_2, P_3)$, in ferroelectric thin films and polycrystalline ceramics. Remarkably, in the general case this task is not tractable by PFM. Indeed, as discussed in the preceding sections, vector PFM measures components of the local electromechanical response vector related to the elements of the piezoelectric tensor, d_{ij}. From these data, either the piezoelectric constants of the material, d_{ij}^0, or a local orientation map, (θ, ψ, φ), can be obtained. At the same time, the conventional approach for measurement of the ferroelectric polarization requires charge measurement during polarization reversal (Smolenskii et al., 1984). The size of the tip–sample contact area renders these measurements almost impossible in PFM due to the extremely small amount of the switching charge (Tiedke & Schmitz, 2004).

In the ideal case, local electromechanical response can be linked to local polarization through the piezoelectric constant tensor, components of which are related to the polarization vector by the Devonshire theory (Smolenskii et al., 1984), $d_{ij} = 2Q_{ijl}P_l$, where Q_{ijl} are components of the electrostriction tensor. This approach is, however, impractical, because the electrostriction tensor is generally unknown and in most cases is derived from piezoelectric measurements. Therefore, in general, PFM is used to map local crystallographic orientation, from which the local polarization orientation is deduced assuming that the relationship between polarization and crystal orientation on the nanoscale is the same as for the macroscopic crystal.

EXPERIMENTAL IMPLEMENTATION OF VECTOR PFM

In this section, we illustrate the applicability of vector PFM imaging and data representation for several materials systems. PFM data has been acquired using a commercial SPM systems (MultiMode NS-IIIA, Veeco Instruments, and Park CP) additionally equipped with external lock-in amplifiers and a function generator (SRS 830 and DS 345; Stanford Research Instruments). To avoid capacitive cross talk, the tip was directly biased through a home-built tip holder. Gold-coated Si probes (NSC-12, spring constant 1–5 N/m; Micromasch) were used. For some measurements, to simultaneously acquire the vertical and lateral amplitude and phase signals, the microscope was additionally equipped with an external computer with LabView software emulating additional signal acquisition channels. The samples studied were $PbTiO_3$ thin films and etched $LaBGeO_5$ glass ceramics. The detailed sample preparation and measurements procedures are described elsewhere (Gupta et al., 2005).

The results of 2D-PFM imaging of the $PbTiO_3$ thin film are shown in Figure 3. There are no markers on the surface and the same location cannot be found after sample rotation, thus precluding 3D-PFM imaging. However, simultaneous acquisition of VPFM and LPFM data allows partial information on local electromechanical properties to be obtained. Shown in Figure 3a,b are vertical and lateral PFM, $A_{1\omega}\cos(\varphi)$ signals, respectively. In the VPFM image, high intensity corresponds to the regions with a strong vertical component of electromechanical response in a positive z direction, whereas low intensity corresponds to a strong response in the negative z direction. Gray areas of intermediate intensity correspond to a weak out-of-plane response component. Similarly, the LPFM image provides information on the in-plane component perpendicular to the cantilever axis, as discussed in the section on electromechanical
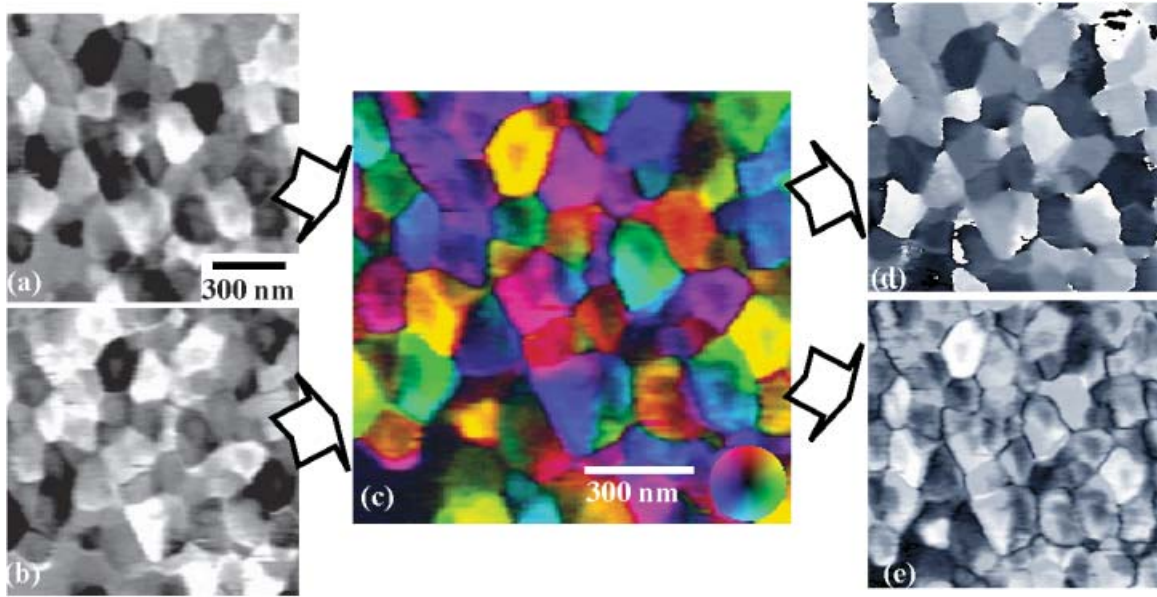
Figure 3. Vertical (**a**) and lateral (**b**) PFM image of PbTiO$_3$ thin film. **c:** Vector representation of 2D PFM data. The orientation angle is coded by the color as reflected in the "color wheel" legend, whereas the intensity provides the magnitude of the response (dark for zero response, bright for strong response). **d:** Angle image. **e:** Amplitude image. Imaging voltage is 1V_{pp}.

measurements above. On close examination, the PFM images in Figure 3a,b show a decrease of the effective PFM signal in the center of the grain (ringlike structure). Such behavior can be attributed to a change in magnitude of the electromechanical response vector, either due to an intrinsic change of the material's properties or tip–surface contact. However, interpretation of separate LPFM and VPFM data is not straightforward.

To address this problem, we employ vector representation for PFM data similar to an approach well known in electron microscopy. The VPFM and LPFM images are normalized with respect to the maximum and minimum values of the signal amplitude so that the intensity changes between -1 and 1, that is, $vpr, lpr \in (-1,1)$. Although not strictly rigorous, this procedure is expected to provide the correct answer for systems in which grains with all possible orientations of the response vector are present, equivalent to using an internal standard. Using commercial software (Mathematika 5.0; Wolfram Research), these 2D vector data are converted to the amplitude/angle pair, $A_{2D} = Abs(vpr + I\,lpr)$, $\theta_{2D} = Arg(vpr + I\,lpr)$. These data are plotted so that the color corresponds to the orientation, whereas color intensity corresponds to the magnitude, as illustrated in Figure 3c. We refer to this method for PFM data representation as a 2D vector PFM image. Note that unlike typical SPM data, where pseudocolors are used to better represent scalar data (e.g., height, friction, intensity, etc.), here both color and intensity convey information and the "color wheel" legend illustrates the direction and magnitude of the response vector.

Notably, the vector PFM image illustrates that color is virtually uniform inside the grains, whereas the intensity varies between the central part of the grain and the circumference. This difference illustrates that only the magnitude, but not the orientation, of the piezoresponse vector changes. This information can be represented in the scalar form by plotting separately phase, θ_{2D}, and magnitude, A_{2D}, data, as illustrated in Figure 3d,e, respectively. In the phase image (Fig. 3d), the phase of the 2D response vector is clearly uniform within individual grains, whereas magnitude (Fig. 3e) changes from the grain center to its circumference.

Vector PFM data in Figure 3c show that the number of individual colors is relatively small. This suggests the existence of preferential electromechanical response orientations, as can be expected for a textured film. Furthermore, this behavior can be seen from the angular distribution histogram shown in Figure 4a. Three broad peaks are clearly seen. The complementary amplitude distribution is shown in Figure 4b.

An example of 3D-PFM imaging is illustrated in Figure 5 using an etched LaBGeO$_5$ glass ceramic. Figure 5a is a topographic image of a ferroelectric grain protruding from the glassy paraelectric phase due to the difference in etching rates. Because of the relatively large grain size ($\sim$50 μm), the same region was imaged several times for different orientations of the cantilever relative to the sample, thus allowing 3D-PFM data to be collected. The VPFM, x-LPFM, and y-LPFM images are shown in Figure 5b,c,d, respectively. These images contain information on all three components of the electromechanical response vector.

To illustrate the possible representations of this data, shown in Figure 6 is the in-plane 2D vector PFM image obtained from a combination of x-LPFM and y-LPFM data
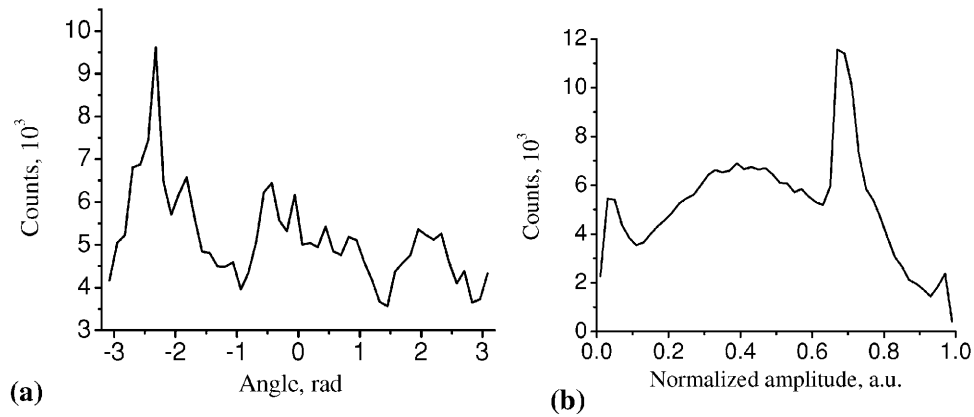
Figure 4. Angle distribution histogram (**a**) and amplitude distribution histogram (**b**) of data in Figure 3d,e indicate the presence of predominant orientations in the film.
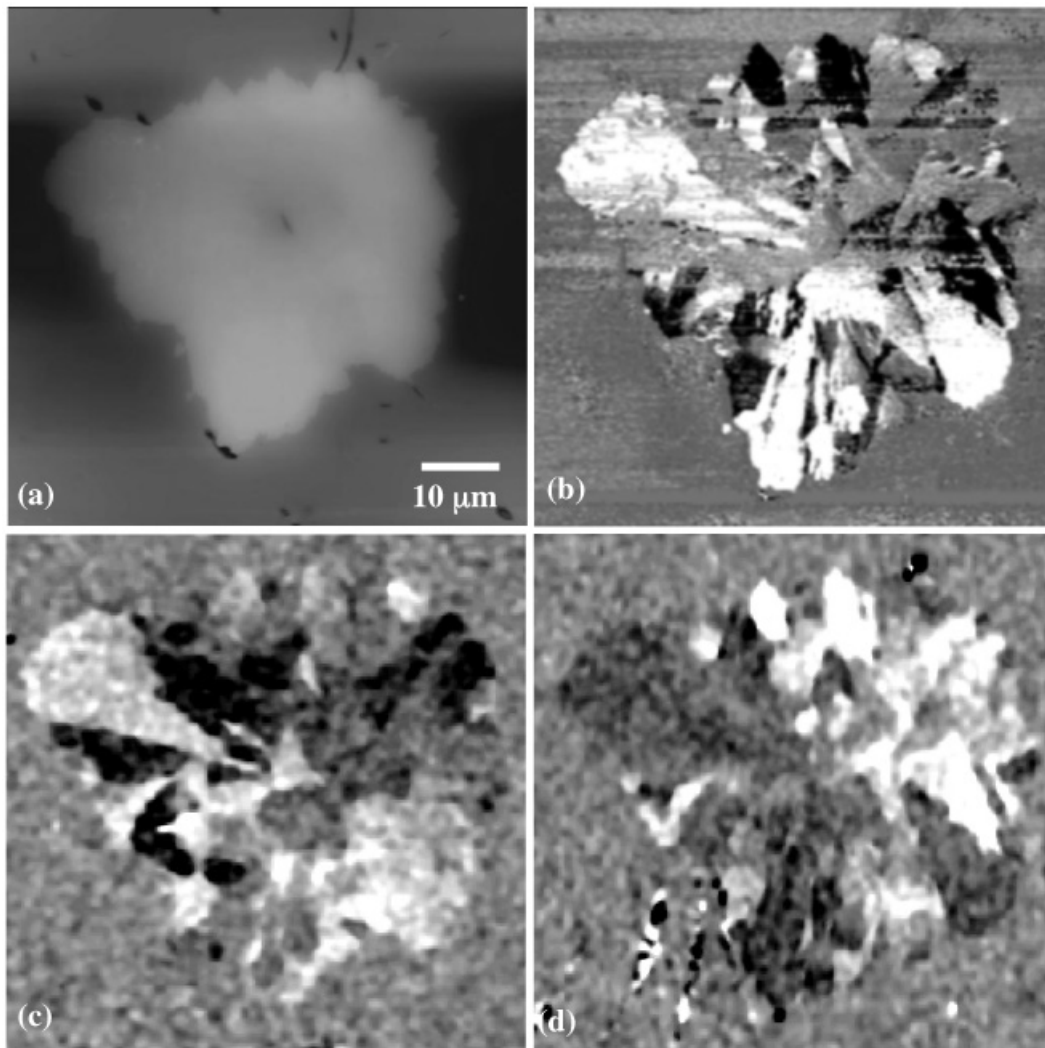
Figure 5. 3D-PFM imaging of ferroelectric $LaBGeO_5$ crystallite in paraelectric glass matrix. **a:** Surface topography; **b:** VPFM; **c:** x-LPFM; and **d:** y-LPFM. Even though images **b**, **c**, and **d** contain full information on electromechanical response vector orientation, data visualization can be improved by using vector imaging as illustrated in Figure 7a,b.
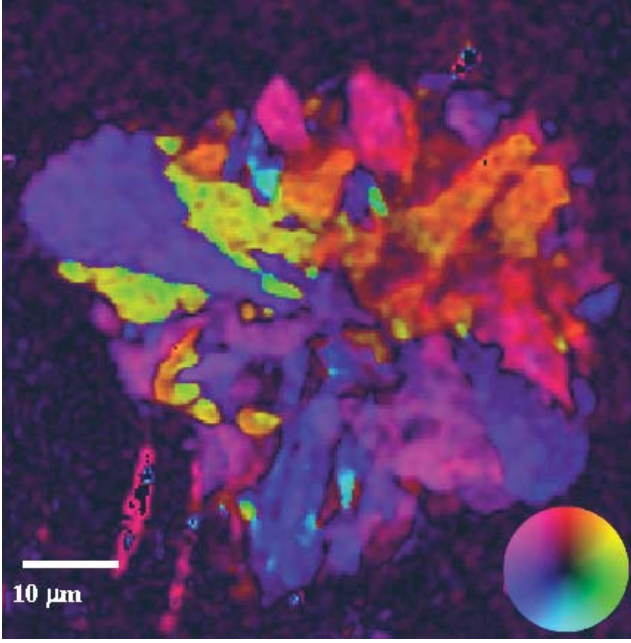
Figure 6. 2D vector PFM image of the same LaBGeO$_5$ crystallite shown in Figure 5. The image contains the information of in-plane orientation of the electromechanical response vector. The orientation angle is coded by the color as reflected in the "color wheel" legend, whereas the intensity provides the magnitude of the response (dark for zero response, bright for strong response).

in Figure 5c,d. Here, the color wheel in Figure 6 directly represents the in-plane orientation of the response vector. Note that Figure 6 represents a true 2D vector image, because relative sensitivities in this case are equal. Similar 2D combinations can be constructed for a combination of x-LPFM and VPFM and y-LPFM and VPFM responses.

The representation of a complete 3D vector field, as opposed to its 2D subset, represents a more challenging problem. Here, the VPFM and x, y-LPFM images are normalized with respect to the maximum and minimum values of the signal amplitude so that the intensity changes between -1 and 1, that is, $vpr, xlpr, ylpr \in (-1,1)$. These 3D vector data $(vpr, xlpr, ylpr)$ are mapped on the red, green, blue color scale, represented as vector (R, G, B), where R, G, and B are mutually orthogonal and vary from 0 to 1. The magnitude of the z component is represented by lightness/darkness, variation in direction in the x, y-plane is given by hue, and the magnitude of the vector is represent by color saturation (note that black and white are colors). The transformation involves rotating the (R, G, B) coordinate system and shifting it so that $(R, G, B) = (0.5, 0.5, 0.5)$ corresponds to zero in the PFM coordinate system, $(vpr, xlpr, ylpr) = (0,0,0)$. This transformation is expressed in the following equation:

$$\begin{pmatrix} R \\ G \\ B \end{pmatrix} = \frac{1}{2}\left(\frac{1}{\sqrt{3}}\left(R_x(\theta_r) \cdot R_z(\phi_r)\right)^T + \begin{pmatrix} 1 \\ 1 \\ 1 \end{pmatrix} \right), \qquad (8)$$
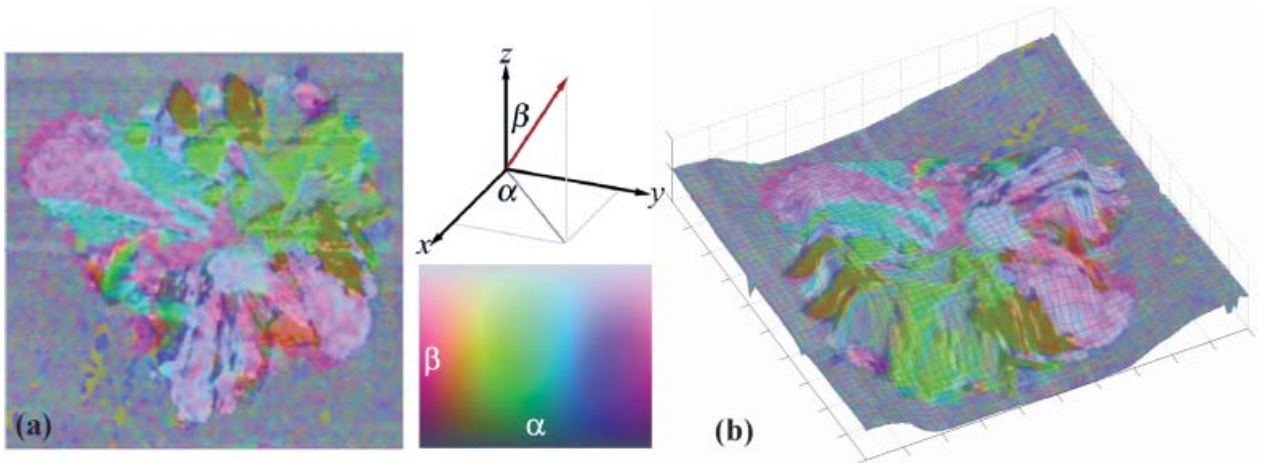
where $R_x(\theta_r)$ and $R_z(\phi_r)$ are rotation matrices

$$R_z(\phi_r) = \begin{pmatrix} \cos\phi_r & \sin\phi_r & 0 \\ -\sin\phi_r & \cos\phi_r & 0 \\ 0 & 0 & 1 \end{pmatrix},$$

$$R_x(\theta_r) = \begin{pmatrix} 1 & 0 & 0 \\ 0 & \cos\theta_r & \sin\theta_r \\ 0 & -\sin\theta_r & \cos\theta_r \end{pmatrix}, \qquad (9a,b)$$

and $\theta_r = \tan^{-1}\sqrt{2}$ and $\phi_r = \pi/4$ are Euler angles.

This coloring scheme applied to the vector data in Figure 5b,c,d yields the color diagram shown in Figure 7a.

Figure 7. a: 3D vector PFM image of the orientation of the electromechanical response vector, as coded by the color map. **b:** Vector PFM data overlaid on a topographic image.

Note that light shading indicates the vector pointing out of the page and dark shading indicates a vector pointing into the page. Gray areas indicate regions where the magnitude of the response vector is relatively small. Intense or saturated hues indicate a strong lateral response with small vertical component. In this representation, vector PFM and topographic data can be correlated by overlaying the color map onto a grid mesh, as illustrated in Figure 7b.

CONCLUSIONS

An approach for vector electromechanical imaging by SPM, referred to as vector-piezoresponse force microscopy, is proposed. The relationship between detected vertical and lateral signal components and the local electromechanical response vector is discussed. An approach for calibration of vector-PFM data is presented and the contribution of longitudinal surface displacement to VPFM data is analyzed. The relationship between 3D-PFM data and local materials' properties is established, and it is shown that 3D PFM can be used as a powerful tool for (a) local electromechanical property measurements on the nanoscale or (b) local orientation imaging on the sub-10-nm level. Finally, several approaches for data representation in 2D-PFM and 3D-PFM are presented. The developed approach can be applied for nanoscale electromechanical characterization of a broad range of material systems including polymers, composites, and biomaterials.

ACKNOWLEDGMENTS

REFERENCES

ABPLANALP, M. (2001). Piezoresponse Scanning Force Microscopy of Ferroelectric Domains. Ph.D. Thesis, Zurich: Swiss Federal Institute of Technology.

ALEXE, M. & GRUVERMAN, A. (2004). *Ferroelectrics at Nanoscale: Scanning Probe Microscopy Approach*. New York: Springer Verlag.

BDIKIN, I.K., SHVARTSMAN, V.V., KIM, S.-H., HERRERO, J.M. & KHOLKIN, A.L. (2004). Frequency-dependent electromechanical response in ferroelectric materials measured via piezoresponse force microscopy. *Mat Res Soc Symp Proc* **784**, C11.3.

CADY, W.G. (1964). *Piezoelectricity: An Introduction to the Theory and Applications of Electromechanical Phenomena in Crystals.* New York: Dover Publications.

CHRISTMAN, J.A., WOOLCOTT, R.R., KINGON, A.I. & NEMANICH, R.J. (1998). Piezoelectric measurements with atomic force microscopy. *Appl Phys Lett* **73**, 3851–3853.

DU, X., BELEGUNDU, U. & UCHINO, K. (1997). Crystal orientation dependence of piezoelectric properties in lead zirconate titanate: Theoretical expectation for thin films. *Jpn J Appl Phys* **36**, 5580–5587.

ENG, L.M., GRAFSTROM, S., LOPPACHER, CH., SCHLAPHOF, F., TROGISCH, S., ROELOFS, A. & WASER, R. (2001). 3-Dimensional electric field probing of ferroelectrics on the nanometer scale using scanning force microscopy. *Adv Solid State Phys* **41**, 287–298.

ENG, L.M., GÜNTHERODT, H.-J., ROSENMAN, G., SKLIAR, A., ORON, M., KATZ, M. & EGER, D. (1998). Nondestructive imaging and characterization of ferroelectric domains in periodically poled crystals. *J Appl Phys* **83**, 5973–5977.

ENG, L.M., GÜNTHERODT, H.-J., SCHNEIDER, G.A., KOPKE, U. & SALDANA, J.M. (1999). Nanoscale reconstruction of surface crystallography from three-dimensional polarization distribution in ferroelectric barium-titanate ceramics. *Appl Phys Lett* **74**, 233–235.

GANPULE, C. (2001). Nanoscale phenomena in ferroelectric thin films. Ph.D. thesis. College Park: University of Maryland.

GANPULE, C.S., STANISHEVSKY, A., AGGARWAL, S., MELNGAILIS, J., WILLIAMS, E., RAMESH, R., JOSHI, V. & PAZ DE ARAUJO, C.A. (1999). Scaling of ferroelectric and piezoelectric properties in Pt/SrBi$_2$Ti$_2$O$_9$/Pt thin films. *Appl Phys Lett* **75**, 3874–3876.

GRUVERMAN, A. (2004). Ferroelectric nanodomains. In *Encyclopedia of Nanoscience and Nanotechnology*, Nalwa, H.S. (Ed.), vol. 3, pp. 359–375. Los Angeles: American Scientific Publishers.

GRUVERMAN, A., AUCIELLO, O. & TOKUMOTO, H. (1996a). Scanning force microscopy for the study of domain structure in ferroelectric thin films. *J Vac Sci Technol B* **14**, 602–605.

GRUVERMAN, A., AUCIELLO, O. & TOKUMOTO, H. (1996b). Scanning force microscopy for the study of domain structure in ferroelectric thin films. *Appl Phys Lett* **69**, 3191–3193.

GRUVERMAN, A., AUCIELLO, O. & TOKUMOTO, H. (1998). Imaging and control of domain structures in ferroelectric thin films via scanning force microscopy. *Annu Rev Mater Sci* **28**, 101–123.

GUPTA, P., JAIN, H., WILLIAMS, D.B., SHIN, J., BADDORF, A.P. & KALININ, S.V. (2005). Observation of ferroelectricity in a confined crystallite using electron-backscattered diffraction and piezoresponse force microscopy. *Appl Phys Lett* **87**, 172903/1–3.

GÜTHNER, P. & DRANSFELD, K. (1992). Local poling of ferroelectric polymers by scanning force microscopy. *Appl Phys Lett* **61**, 1137–1140.

HARNAGEA, C. (2001). Local piezoelectric response and domian structures in ferroelectric thin films investigated by voltage modulated force microscopy. Dr. Rer. Nat. thesis, Halle: Martin-Luther-Universität Halle Wittenberg.

HARNAGEA, C., ALEXE, M., HESSE, D. & PIGNOLET, A. (2003). Contact resonances in voltage-modulated force microscopy. *Appl Phys Lett* **83**, 338–341.

HARNAGEA, C., PIGNOLET, A., ALEXE, M. & HESSE, H. (2001). Piezoresponse scanning force microscopy: What quantitative informa-

tion can we really get out of piezoresponse measurements on ferroelectric thin films. *Integrated Ferroelectrics* **38**, 667–673.

Hong, S. (2004). *Nanoscale Phenomena in Ferroelectric Thin Films*. Boston: Kluwer Academic Publishers.

Hong, S., Woo, J., Shin, H., Jeon, J.U., Pak, Y.E., Colla, E.L., Setter, N., Kim, E. & No, K. (2001). Principle of ferroelectric domain imaging using atomic force microscope. *J Appl Phys* **89**, 1377–1386.

Huey, B.D., Ramanujan, C., Bobji, M., Blendell, J., White, G., Szoszkiewicz, R. & Kulik, A. (2004). The importance of distributed loading and cantilever angle in piezo-force microscopy. *J Electroceramics* **13**, 287–291.

Jeon, S., Braiman, Y. & Thundat, T. (2004). Cross talk between bending, twisting, and buckling modes of three types of microcantilever sensors. *Rev Sci Instrum* **75**, 4841–4845.

Kalinin, S.V. (2002). Nanoscale phenomena at oxide surfaces and interfaces by scanning probe microscopy. Ph.D. Thesis, Philadelphia, PA: University of Pennsylvania.

Kalinin, S.V. & Bonnell, D.A. (2001). Local potential and polarization screening on ferroelectric surfaces. *Phys Rev B* **63**, 125411/1–13.

Kalinin, S.V. & Bonnell, D.A. (2002). Imaging mechanism of piezoresponse force microscopy of ferroelectric surfaces. *Phys Rev B* **65**, 125408/1–11.

Kalinin, S.V. & Bonnell, D.A. (2004). Electric scanning probe imaging and modification of ferroelectric surfaces. In *Ferroelectrics at Nanoscale: Scanning Probe Microscopy Approach*, Alexe, M., and Gruverman, A. (Eds.), pp. 1–43. New York: Springer Verlag.

Kalinin, S.V., Karapetian, E. & Kachanov, M. (2004). Nanoelectromechanics of piezoresponse force microscopy. *Phys Rev B* **70**, 184101/1-24.

Kalinin, S.V., Rodriguez, B.J., Shin, J., Jesse, S., Grichko, V., Thundat, T., Baddorf, A.P. & Gruverman, A. (2006). Bioelectromechanical imaging by scanning probe microscopy: Galvani's experiment at the nanoscale. *Ultramicroscopy* **106**, 334–340.

Karapetian, E., Kachanov, M. & Kalinin, S.V. (2005). Nanoelectromechanics of piezoelectric indentation and applications to scanning probe microscopies of ferroelectric materials. *Phil Mag* **85**, 1017–1051.

Karapetian, E., Kachanov, M. & Sevostianov, I. (2002). The principle of correspondence between elastic and piezoelectric problems. *Arch Appl Mech* **72**, 564–587.

Li, J.-H., Chen, L., Nagarajan, V., Ramesh, R. & Roytburd, A.L. (2004). Finite element modeling of piezoresponse in nanostructured ferroelectric films. *Appl Phys Lett* **84**, 2626–2628.

More, N., Ramond, M. & Tordjeman, Ph. (2005). Cantilever calibration for nanofriction experiments with atomic force microscope. *Appl Phys Lett* **86**, 163103/1–3.

Munoz-Saldana, J., Hoffmann, M.J. & Schneider, G.A. (2003). Ferroelectric domains in coarse-grained lead zirconate titanate ceramics characterized by scanning force microscopy. *J Mater Res* **18**, 1777–1786.

Nagarajan, V., Roytburd, A., Stanishevsky, A., Prasertchoung, S., Zhao, T., Chen, L., Melngailis, J., Auciello, O. & Ramesh, R. (2003). Dynamics of ferroelastic domains in ferroelectric thin films. *Nat Mater* **2**, 43–47.

Newnham, R.E. (2005). *Properties of Materials: Anisotropy, Symmetry, Structure*. New York: Oxford University Press.

Nye, J.F. (1985). *Physical Properties of Crystals*. New York: Oxford University Press.

Ogletree, D.F., Carpick, R.W. & Salmeron, M. (1996). Calibration of frictional forces in atomic force microscopy. *Rev Sci Instrum* **67**, 3298–3306.

Ouyang, J., Yang, S.Y., Chen, L., Ramesh, R. & Roytburd, A.L. (2004). Orientation dependence of the converse piezoelectric constants for epitaxial single domain ferroelectric films. *Appl Phys Lett* **85**, 278–280.

Peter, F., Rüdiger, A., Waser, R., Szot, K. & Reichenberg, B. (2005). Comparison of in-plane and out-of-plane optical amplification in AFM measurements. *Rev Sci Instrum* **76**, 046101/1–3.

Rabe, U., Kopycinska, M., Hiserkorn, S., Munoz-Saldana, J., Schneider, G.A. & Arnold, W. (2002). High-resolution characterization of piezoelectric ceramics by ultrasonic scanning force microscopy techniques. *J Phys D* **35**, 2621–2635.

Rodriguez, B.J., Gruverman, A., Kingon, A.I., Nemanich, R.J. & Cross, J.S. (2004). Three-dimensional high-resolution reconstruction of polarization in ferroelectric capacitors by piezoresponse force microscopy. *J Appl Phys* **95**, 1958–1962.

Roelofs, A., Böttger, U., Waser, R., Schlaphof, F., Trogisch, S. & Eng, L.M. (2000). Differentiating 180° and 90° switching of ferroelectric domains with three-dimensional piezoresponse force microscopy. *Appl Phys Lett* **77**, 3444–3446.

Sarid, D. (1991). *Scanning Force Microscopy*. New York: Oxford University Press.

Smolenskii, G.A., Bokov, V.A., Isupov, V.A., Krainik, N.N., Pasynkov, R.E. & Sokolov, A.I. (1984). *Ferroelectrics and Related Materials*. New York: Cordon and Breach.

Tiedke, S. & Schmitz, T. (2004). Electrical characterization of nanoscale ferroelectric structures. In *Ferroelectrics at Nanoscale: Scanning Probe Microscopy Approach*, Alexe, M. and Gruverman, A. (Eds.), pp. 87–114. New York: Springer Verlag.

Appendix A

To relate the bias-induced strain to displacement, we consider the mechanics of a free-standing uniform piezoelectric capacitor of thickness, h, with electrodes on the top and bottom surfaces. The bias, V, is applied between the electrodes such that the field across the material is $\mathbf{E} = E_3\mathbf{z}$, where $E_3 = V/h$. The field results in the uniform strain in the material, and equation (3) yields the following system of partial differential equations for the components of deformation vector:

$$X_{11} = \frac{\partial u_1}{\partial x_1} = d_{31} E_3 = k_1 \tag{A1}$$

$$X_{22} = \frac{\partial u_2}{\partial x_2} = d_{32} E_3 = k_2 \tag{A2}$$

$$X_{33} = \frac{\partial u_3}{\partial x_3} = d_{33} E_3 = k_3 \tag{A3}$$

$$X_{12} = \frac{1}{2}\left(\frac{\partial u_1}{\partial x_2} + \frac{\partial u_2}{\partial x_1}\right) = d_{36}\,E_3 = \frac{1}{2}\,m_1 \qquad \text{(A4)}$$

$$X_{13} = \frac{1}{2}\left(\frac{\partial u_1}{\partial x_3} + \frac{\partial u_3}{\partial x_1}\right) = d_{35}\,E_3 = \frac{1}{2}\,m_2 \qquad \text{(A5)}$$

$$X_{23} = \frac{1}{2}\left(\frac{\partial u_2}{\partial x_3} + \frac{\partial u_3}{\partial x_2}\right) = d_{34}\,E_3 = \frac{1}{2}\,m_3. \qquad \text{(A6)}$$

The solution for this system can be found as

$$u_1 = k_1 x_1 + b_2 x_2 + b_3 x_3 + C_1 \qquad \text{(A7)}$$

$$u_2 = (m_1 - b_2)x_1 + k_2 x_2 + b_1 x_3 + C_2 \qquad \text{(A8)}$$

$$u_3 = (m_2 - b_3)x_1 + (m_3 - b_1)x_2 + k_3 x_3 + C_3 \qquad \text{(A9)}$$

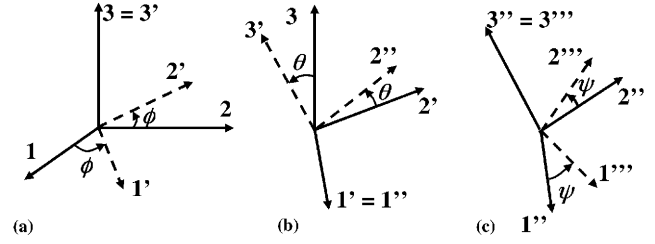where b_i and C_i, $i = 1,\ldots,3$ are constants determined by boundary conditions.

From boundary conditions on the lower plane $u_3(x_1, x_2, 0) = 0$, $u_1(0,0,0) = 0$, and $u_2(0,0,0) = 0$, the constants can be found as $m_2 = b_3$, $m_3 = b_1$, $m_1 = b_2$, and $C_i = 0$. Thus, the displacement field is given by

$$u_1 = k_1 x_1 + m_1 x_2 + m_2 x_3 \qquad \text{(A10)}$$

$$u_2 = k_2 x_2 + m_3 x_3 \qquad \text{(A11)}$$

$$u_3 = k_3 x_3. \qquad \text{(A12)}$$

Figure B1. Coordinate transformations for transition from the crystal to the laboratory coordinate systems. **a:** Counterclockwise rotation of ϕ about axis 3. **b:** Counterclockwise rotation of θ about axis 1′. **c:** Counterclockwise rotation of ψ about axis 3″.

Due to the radial symmetry of the field produced by the PFM tip, the PFM signal is approximated by the displacement in the center of the top plane. For $x_1 = x_2 = 0$ and $x_3 = h$, the components of the displacement vector are

$$u_1 = m_2 c = d_{35}\,E_3\,c = d_{35}\,V \qquad \text{(A13)}$$

$$u_2 = k_2 x_2 + m_3 x_3 = d_{34}\,E_3\,c = d_{34}\,V \qquad \text{(A14)}$$

$$u_3 = k_3 x_3 = d_{33}\,E_3\,c = d_{33}\,V. \qquad \text{(A15)}$$

Thus, the in-plane component of surface displacement measured in the LPFM experiment is directly related to the shear components, d_{34} and d_{35}, of the piezoelectric constant tensor, whereas components d_{31} and d_{32} result in radial expansion and contraction symmetric with respect to the tip. The normal component of the PFM signal is given by d_{33}, as expected from simple theory.

Appendix B

The complete description of the rotation dependence of the 3D-PFM signal requires rotation of the piezoelectric constant tensor. The rotations are by angles ϕ, θ, ψ as shown in Figure B1. The rotation matrix is $A_{ij} = (a_{ij})$;

$$A_{ij} = \begin{pmatrix} (\cos\phi\cos\psi - \cos\theta\sin\phi\sin\psi) & (\cos\phi\sin\psi + \cos\theta\cos\phi\sin\psi) & \sin\theta\sin\psi \\ (-\cos\theta\cos\psi\sin\phi - \cos\phi\sin\psi) & (\cos\theta\cos\phi\cos\psi - \sin\phi\sin\psi) & \cos\theta\sin\psi \\ \sin\theta\sin\phi & -\cos\phi\sin\theta & \cos\theta \end{pmatrix}. \qquad \text{(B1)}$$

The elements of N_{ij} matrix in equation (4) are

$$N_{ij} = \begin{vmatrix} a_{11}^2 & a_{21}^2 & a_{31}^2 & 2a_{21}a_{31} & 2a_{31}a_{11} & 2a_{11}a_{21} \\ a_{12}^2 & a_{22}^2 & a_{32}^2 & 2a_{22}a_{32} & 2a_{32}a_{12} & 2a_{12}a_{22} \\ a_{13}^2 & a_{23}^2 & a_{33}^2 & 2a_{23}a_{33} & 2a_{33}a_{13} & 2a_{13}a_{23} \\ a_{12}a_{13} & a_{22}a_{23} & a_{32}a_{33} & a_{22}a_{33} + a_{32}a_{23} & a_{12}a_{33} + a_{32}a_{13} & a_{22}a_{13} + a_{12}a_{23} \\ a_{13}a_{11} & a_{23}a_{21} & a_{33}a_{31} & a_{21}a_{33} + a_{31}a_{23} & a_{31}a_{13} + a_{11}a_{33} & a_{11}a_{23} + a_{21}a_{13} \\ a_{11}a_{12} & a_{21}a_{22} & a_{31}a_{32} & a_{21}a_{32} + a_{31}a_{22} & a_{31}a_{12} + a_{11}a_{32} & a_{11}a_{22} + a_{21}a_{12} \end{vmatrix}. \qquad \text{(B2)}$$